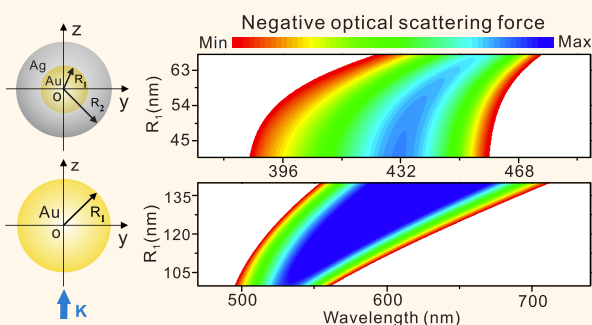


# Fano Resonance-Induced Negative Optical Scattering Force on Plasmonic Nanoparticles

Huajin Chen,<sup>†,\*</sup> Shiyang Liu,<sup>\*,†,§</sup> Jian Zi,<sup>†,\*</sup> and Zhifang Lin<sup>\*,†,⊥</sup>

<sup>†</sup>State Key Laboratory of Surface Physics (SKLSP) and Department of Physics, Fudan University, Shanghai 200433, China, <sup>‡</sup>Key Laboratory of Micro and Nano Photonic Structures (MOE), Fudan University, Shanghai 200433, China, <sup>§</sup>Institute of Information Optics, Zhejiang Normal University, Jinhua, Zhejiang 321004, China, and <sup>⊥</sup>Collaborative Innovation Center of Advanced Microstructures, Nanjing University, Nanjing 210093, China

**ABSTRACT** We demonstrate theoretically that Fano resonance can induce a negative optical scattering force acting on plasmonic nanoparticles in the visible light spectrum when an appropriate manipulating laser beam is adopted. Under the illumination of a zeroth-order Bessel beam, the plasmonic nanoparticle at its Fano resonance exhibits a much stronger forward scattering than backward scattering and consequently leads to a net longitudinal backward optical scattering force, termed Fano resonance-induced negative optical scattering force. The extinction spectra obtained based on the Mie theory show that the Fano resonance arises from the interference of simultaneously excited multipoles, which can be either a broad electric dipole mode and a narrow electric quadrupole mode, or a quadrupole and an octupole mode mediated by the broad electric dipole. Such Fano resonance-induced negative optical scattering force is demonstrated to occur for core–shell, homogeneous, and hollow metallic particles and can therefore be expected to be universal for many other nanostructures exhibiting Fano resonance, adding considerably to the flexibility of optical micromanipulation on the plasmonic nanoparticles. More interestingly, the flexible tunability of the Fano resonance by particle morphology opens up the possibility of tailoring the optical scattering force accordingly, offering an additional degree of freedom to optical selection and sorting of plasmonic nanoparticles.



**KEYWORDS:** Fano resonance · negative optical scattering force · extinction spectra · plasmonics · optical selection

Optical micromanipulation based on optical forces<sup>1–6</sup> due to the light–matter interaction has found a variety of vital applications ranging from physics,<sup>7–13</sup> to chemistry,<sup>14–16</sup> to biology.<sup>17–20</sup> Among all these interdisciplinary applications, optical tweezers, which are based upon optical trapping due largely to the gradient force originating from inhomogeneity of the optical field, play a dominant part<sup>1–6,10–14,18–21</sup> and have been developed into an indispensable tool for contactless confinement of small particles or control of the position of a mesoscopic object up to submicro- and even nanometric precision.<sup>21</sup> Optical force basically falls into two categories: the gradient force and the scattering force (the latter includes absorption force). The former can be written as a gradient of a scalar function  $\phi(\mathbf{r})$  of optical fields. As such the gradient force generally traps, favoring optical confinement

by equilibrating an object at the extremum of  $\phi(\mathbf{r})$ . On the other hand, the scattering force typically transports, since it usually pushes particles forward along the propagation of light, destabilizing optical trapping. A metallic plasmonic particle, quite like a high-refractive-index particle, is more difficult to trap, because the refractive index mismatch between the trapped particle and its surrounding medium causes strong backscattering and increases the scattering force, resulting in a deterioration of the trapping efficiency. So some elegant methods were proposed to reduce backscattered light by photonically modulating the object to be trapped,<sup>22–24</sup> among which an antireflection coating is the simplest and most efficient way, by which single-beam optical trapping of a high-refractive-index particle with a trapping force greater than a nanonewton has been achieved.<sup>24</sup> Here we propose an alternative scenario to attenuate the forward

\* Address correspondence to syliu@zjnu.cn, phlin@fudan.edu.cn.

Received for review December 1, 2014 and accepted January 29, 2015.

Published online January 29, 2015  
10.1021/nn506835j

© 2015 American Chemical Society

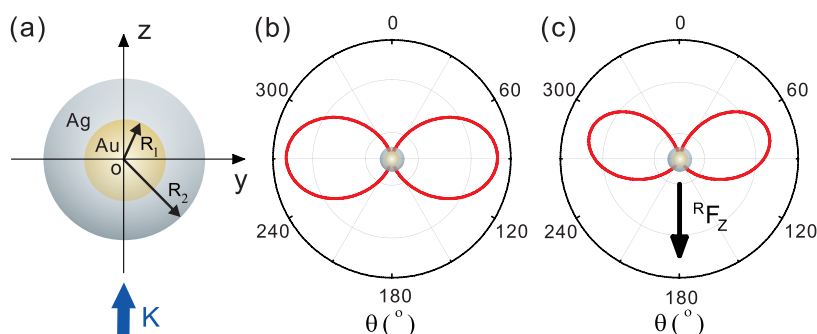


**Figure 1.** (a) Schematic representation of a core–shell nanoparticle. (b and c) Scattering intensity  $S(\theta)$  for a Au–Ag core–shell particle at an incident wavelength of  $\lambda = 635$  nm (b) and  $\lambda = 392$  nm (c) under the illumination of a zeroth-order TM-polarized Bessel beam propagating along the  $z$  axis with a cone angle of  $\alpha = 78^\circ$  and a field intensity at the beam axis of  $I(0) = 100$  mW/ $\mu\text{m}^2$ . The core and shell radii of the particle are  $R_1 = 40$  nm and  $R_2 = 80$  nm, respectively. The particle is positioned on the beam axis. The surrounding medium is water with the refractive index  $n_{\text{ref}} = 1.33$ . The black arrow in (c) denotes the resulting backward recoil force that dominates over the incident force and brings about the net NOSF that tends to pull the particle all the way toward the light source.

scattering force, that is, through enhancing the forward scattering by taking advantage of Fano resonance of the plasmonic particles.

Fano resonances,<sup>25</sup> arising from the interference between a narrow discrete resonance and a broad continuum state, have been extensively observed and studied in physical, chemical, and biological sciences in recent decades.<sup>26–28</sup> In particular, with the advent of plasmonics and metamaterials, Fano resonances in plasmonic nanostructures, including single metallic particles,<sup>29,30</sup> core–shell nanoparticles,<sup>31–33</sup> ring/disk cavities,<sup>34,35</sup> plasmonic nanoparticle clusters,<sup>36–38</sup> and other plasmonic nanostructures,<sup>39–41</sup> have received considerable attention, owing to their flexibly tunable resonance and dramatically enhanced plasmon field. While a great deal of effort has been focused on the promising applications of Fano resonances in biosensing,<sup>35,42</sup> surface-enhanced Raman scattering,<sup>43,44</sup> optical switching,<sup>45,46</sup> plasmon-induced transparency,<sup>31,47</sup> and many others,<sup>48–51</sup> much less attention is devoted to its effect on optical force for optical manipulation. Some exceptions are those examining the optical force transverse to the direction of light propagation<sup>52–54</sup> and the one studying laser cooling associated with Fano resonance.<sup>55</sup> The role of Fano resonances in tailoring longitudinal optical scattering force for optical manipulation, however, has been left largely unexplored.

In this theoretical paper, our effort is devoted to investigating the effect of Fano interference on tailoring the longitudinal scattering force acting on plasmonic nanoparticles. To focus solely on the scattering force, our study takes a zeroth-order Bessel beam with transverse magnetic (TM) polarization as the incident beam,<sup>56–59</sup> due to its propagation-invariant characteristic. We start with a Au–Ag core–shell nanoparticle for the convenience of physical illustration. For the broad single dipolar resonance, the Au–Ag core–shell nanoparticle exhibits a nearly symmetric forward and backward scattering intensity distribution, and the longitudinal scattering force is along the beam

propagation direction, as usual. When approaching the Fano resonance, an asymmetric scattering diagram develops, where forward scattering is significantly enhanced, while the backscattered light is considerably reduced, leading to a substantial attenuation of forward scattering force along the direction of light propagation and, more interestingly, even resulting in a net negative optical scattering force (NOSF), which has recently stimulated burgeoning research activities,<sup>60–67</sup> for its anomalous pulling action opposite the flow of light, and thus adds a novel degree of freedom to optical manipulation, in addition to the well-known optical propulsion and trapping. The calculations of extinction efficiency spectra for the core–shell particle based on the Mie theory<sup>68</sup> reveal that the Fano resonance originates from the coupling of a broad bright dipole mode with the narrow dark quadrupole and octupole modes. Such a multipolar Fano resonance and the induced NOSF are demonstrated for both homogeneous and hollow metallic particles and thus can be anticipated universally for other nanostructures exhibiting Fano resonance, rendering the optical micromanipulation of the plasmonic nanoparticles much more versatile. More importantly, the flexible tunability of Fano resonance enables an effective tailoring of the optical scattering force, either forward or backward, accordingly, which may contribute significantly to the development of optical manipulation of plasmonic nanoparticles.

## RESULTS AND DISCUSSION

We start our discussion with the scattering properties of a Au–Ag core–shell nanoparticle, which can be synthesized through simple chemical reduction techniques.<sup>32</sup> The schematic representation is illustrated in Figure 1a, where  $R_1$  and  $R_2$  denote the radius of the Au core and Ag shell, respectively. In our calculations, we assume that the particle is embedded in water with the refractive index  $n_{\text{ref}} = 1.33$  and is illuminated by a zeroth-order Bessel beam of TM polarization<sup>56,57</sup> with

a magnetic field perpendicular to the propagating direction along  $z$ . The particle is positioned on the beam axis so that it is subjected solely to the scattering force due to the propagation-invariant characteristic of the Bessel beam.<sup>56–59</sup> The electric field of the Bessel beam is given in eq 4 in the Methods section, and its intensity at the beam axis is taken as  $100 \text{ mW}/\mu\text{m}^2$  throughout this paper. The scattering problem of the particle is solved based on the generalized Lorenz–Mie theory<sup>69</sup> with analytically derived beam shape coefficients (see Methods).<sup>70,71</sup> Typical far-field scattering intensity distributions of the Au–Ag particle are shown in Figure 1b and c, for the single dipole resonance at the incident wavelength  $\lambda = 635 \text{ nm}$  and the dip of the Fano resonance at  $\lambda = 392 \text{ nm}$ , respectively. The normalized scattering intensity is defined in eq 11 in the Methods, which is independent of the azimuthal angle due to the azimuthal symmetry. In our calculation, the circular frequency  $\omega$ -dependent permittivities of Au and Ag are evaluated using Drude's dielectric function<sup>72,73</sup>  $\varepsilon(\omega) = \varepsilon_\infty - \omega_p^2/(\omega^2 + i\omega\gamma)$ , where  $\varepsilon_\infty$  is the high-frequency-limit dielectric constant,  $\gamma$  is the damping constant, and  $\omega_p$  is the plasmon resonance frequency. We use the best fit parameters<sup>32</sup> of Au and Ag obtained from the experimental dielectric functions.<sup>74</sup> Figure 1b shows a nearly symmetric forward and backward distribution of far-field scattering energy around the particle, inducing nearly vanishing backward recoil force in the proximity of the single dipolar resonance, which will be further manifested in Figure 2a. As the incident frequency increases, the multipolar Fano interference comes into play and a forward-tilted scattering pattern develops, as typically visualized, at the dip of the Fano resonance at  $\lambda = 392 \text{ nm}$ , in Figure 1c. This obviously forward-directed scattering results in an enhanced backward recoil force  ${}^R F_z$  in the longitudinal  $z$  direction, denoted by a black arrow, suggesting a possibility of tuning the scattering force by the Fano resonance.

To illustrate the Fano resonance-tailored optical scattering force exerting on the Au–Ag core–shell nanoparticle, we calculate the optical force as a function of the incident wavelength  $\lambda$  based on the generalized Lorenz–Mie scattering theory and the Maxwell stress tensor approach.<sup>75–77</sup> An explicit expression for the longitudinal optical force is given by eq 14 in the Methods, where the total optical scattering force  $F_z$  is decomposed into the incident force  ${}^I F_z$  and the recoil force  ${}^R F_z$ .<sup>61</sup> Physically, the incident term  ${}^I F_z$  arises from the interaction of the excited multipoles with the incident field, which is always positive due to momentum transfer from the incident photons. The recoil term  ${}^R F_z$ , on the other hand, comes from the interference of the adjacent multipoles excited on the nanoparticle, possibly inducing a negative optical force. For simplicity, we do not present the equations and results for the transverse optical force since it

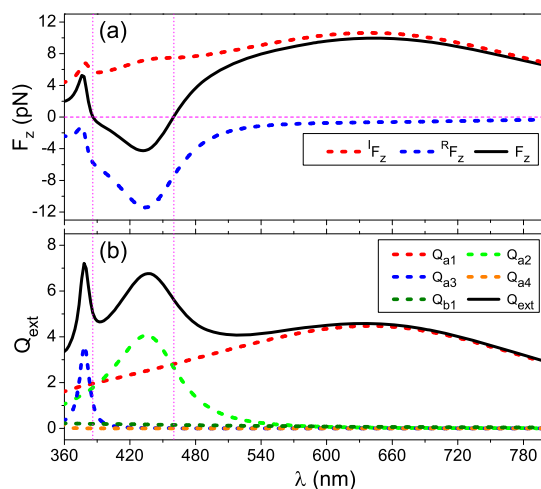


**Figure 2.** Longitudinal incident force  ${}^I F_z$  and the recoil force  ${}^R F_z$ , defined by eq 14 in the Methods, acting on a Au–Ag core–shell nanoparticle (a) and the total extinction efficiency  $Q_{\text{ext}}$  and partial extinction efficiency  $Q_{a_n}$ ,  $Q_{b_n}$  (b) as functions of the incident wavelength  $\lambda$ , indicating that the NOSF is induced by the Fano interference between different plasmon modes excited in the particle, while the interference between narrow adjacent quadrupole and octupole dark modes is mediated by the broad electric dipole mode. All other parameters are the same as those in Figure 1 except for a plane wave incidence in part b.

vanishes due to the azimuthal symmetry. The calculated longitudinal scattering optical force is displayed in Figure 2 together with the total and partial extinction efficiency  $Q_{\text{ext}}$ . It can be observed in Figure 2a that as the incident frequency increases and the Fano interference is brought into play, the negative recoil force  ${}^R F_z$  (blue line) is significantly enhanced, while the positive-definite incident force  ${}^I F_z$  (red line) remains relatively inert to the change of the incident frequency, leading to a sharp decrease of the total scattering force  $F_z$  (black line) when approaching Fano interference. In the proximity of the dip of the Fano resonance, the backward recoil force surpasses the forward incident force, yielding a remarkable net negative optical force ranging nearly from 390 to 460 nm in the visible light spectrum.

To confirm the relationship between the net NOSF and the Fano interference, we present in Figure 2b the partial as well as the total extinction efficiency spectra *versus* the incident wavelength. For a general spherical particle subject to a plane wave incidence, the extinction efficiency can be evaluated according to<sup>68</sup>

$$Q_{\text{ext}} = \sum_{n=1}^{\infty} (Q_{a_n} + Q_{b_n}) \quad (1)$$

with

$$Q_{a_n} = \frac{2(2n+1)}{(kR)^2} \text{Re}(a_n),$$

$$Q_{b_n} = \frac{2(2n+1)}{(kR)^2} \text{Re}(b_n) \quad (2)$$

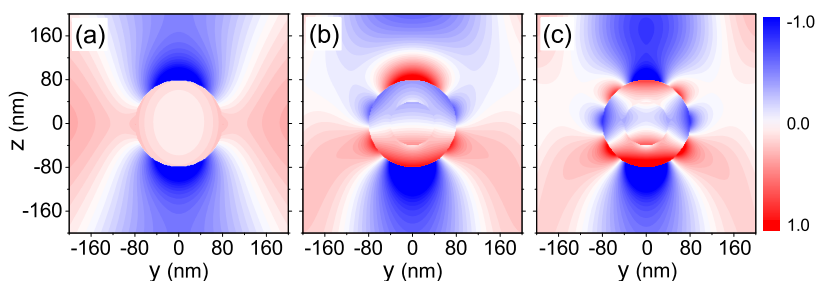


**Figure 3.** Near-field plots of the  $z$ -component of the electric field for a Au–Ag core–shell particle excited at the wavelength (a)  $\lambda = 635$  nm (dipole peak), (b)  $\lambda = 430$  nm (quadrupole peak), and (c)  $\lambda = 392$  nm (Fano dip) under the illumination of a zeroth-order TM-polarized Bessel beam propagating along the  $z$  axis.

where  $a_n$  and  $b_n$  are Mie scattering coefficients<sup>68</sup> associated with the electric and magnetic multipolar modes, respectively,  $k$  is the wavenumber in the background, and  $R$  is the particle radius. In the plasmonic Fano resonances, generally, the dipolar mode of a single particle is a bright mode, while the higher order resonances are dark modes.<sup>26–28</sup> In the small particle limit with  $R \ll \lambda$  in the range from 540 to 800 nm, the total extinction spectra denoted by the black solid line in Figure 2b is dominated by the contribution from the dipole mode. Compared with Figure 2a, the corresponding optical force is positive because the recoil force  ${}^R F_z$  is nearly vanishing, due to the rough backward and forward symmetry of scattering; see Figure 1a. As the wavelength decreases, the electric quadrupole mode makes its appearance, as shown by the green dashed line, leading to an enhancement of backward recoil force and thus a sharp decrease of the total scattering force. The situation evolves further as the Fano interference between the dark electric quadrupole mode and the bright dipolar mode is intensified in the vicinity of the quadrupole resonance, resulting in a predominance of the recoil force  ${}^R F_z$  over the incident force  ${}^I F_z$  and thus bringing about a net NOSF. As the incident wavelength decreases further, a prominent asymmetric dip emerges at  $\lambda = 392$  nm, originating from the interference between the adjacent quadrupole and octupole modes mediated by the bright plasmonic dipolar mode, as manifested by the broad peak of partial extinction efficiency from the dipole excitation (see the red dashed line in Figure 2b). When an appropriate incident beam is adopted, this Fano dip may roughly signify a possible onset of a net NOSF on a plasmonic particle at the higher frequency end, while the NOSF occurs in a range from about 390 to 460 nm, caused by the dipole–quadrupole and quadrupole–octupole Fano interference.<sup>54</sup> A pictorial demonstration of the excitation and interference of the multipole modes can be visualized by the near-field maps shown in Figure 3, where one can observe the excitation of dipole resonance, dipole–quadrupole interference, and dipole-mediated quadrupole–octupole interference, illustrated in panels a, b, and c, respectively.

It is noted that a negative recoil term  ${}^R F_z$  with large magnitude in the proximity of a Fano resonance does not necessarily bring about an NOSF. The occurrence of an NOSF also requires an appropriately devised manipulating optical beam. For a single plane wave, the positive definite incident term  ${}^I F_z$  always surpasses the recoil term  ${}^R F_z$ , ruling out any possibility of NOSF even at a Fano resonance. To diminish the incident term  ${}^I F_z$ , we need to engineer an optical beam such that it consists of only planar modes with a large transverse component of the wave vector, as was previously analyzed.<sup>61</sup> Bessel beams with a large cone angle are typical examples that satisfy this requirement. A pair of glancing coherent plane waves may be the simplest optical field for this purpose, as has been corroborated both theoretically and experimentally.<sup>61,67</sup> In any case, the Fano resonance offers a great chance to achieve an NOSF provided that the manipulating beam is devised to meet the above requirement.

The Fano resonance-induced NOSF is not solely limited to core–shell particles. It is quite universal in the sense that it also occurs for homogeneous and hollow metallic particles, enabling an alternative tool for optical manipulation of plasmonic particles, which, like high-refractive-index particles, are usually difficult to trap by a single gradient trap due to strong forward scattering force. Figure 4a shows the longitudinal incident force  ${}^I F_z$ , recoil force  ${}^R F_z$ , and the total scattering force  $F_z$  on a homogeneous Au particle of radius  $R = 110$  nm when it is immersed on the beam axis of a zeroth-order TM-polarized Bessel beam. It can be seen that a notable net NOSF can be induced in the range from 505 to 596 nm, originating from the same physical mechanism, as can be established from the total and partial extinction efficiency spectra displayed in Figure 4b. That is, a net NOSF comes about within the frequency range of the Fano interference between the broad dipole mode and the narrow quadrupole resonance and between the quadrupole and octupole modes, with the latter coordinated by the broad dipole state. Compared with Figure 2, the optical force on the homogeneous Au nanoparticle has a larger magnitude and the Fano dip exhibits a red shift to

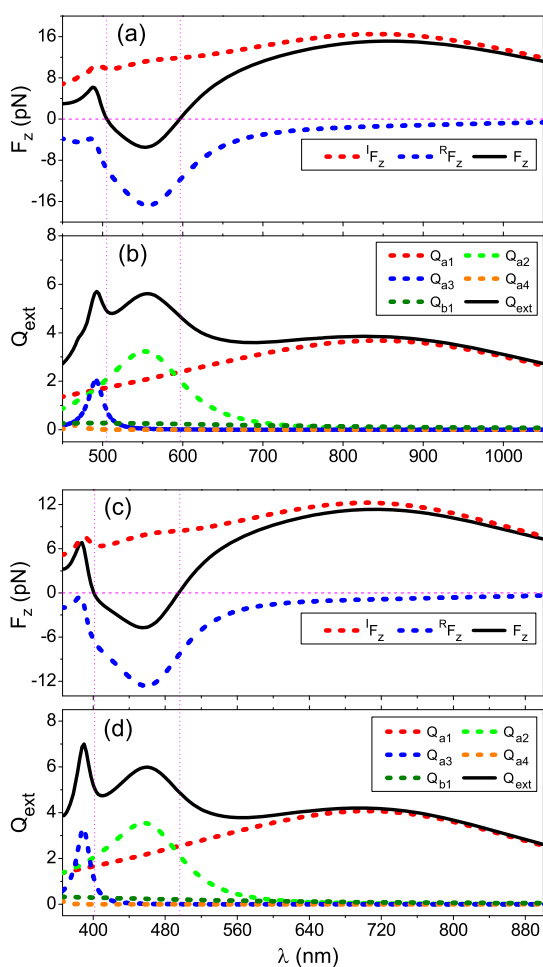


**Figure 4.** Same as Figure 2, except that a homogeneous Au nanoparticle (a, b) and a hollow Ag shell particle (c, d) are considered. The homogeneous Au nanoparticle has the radius  $R_1 = 110$  nm, and the hollow Ag particle has the empty core of radius  $R_1 = 40$  nm and the outer radius  $R_2 = 90$  nm.

$\lambda = 510$  nm because of the larger particle size and the relatively lower frequency response of surface plasmons of Au. The NOSF can be easily realized for the Au particle with a diameter of around one-third of the working wavelength at the plasmonic resonance, suggesting a promising way to decrease the forward scattering force that hinders the flexible trapping of such gold nanoparticles close to the plasmon resonance frequency.<sup>78</sup>

Similarly, the multipolar Fano interference-induced net NOSF also manifests itself on a single hollow Ag shell, as typically shown in Figure 4c. For a Ag shell a remarkable NOSF appears in the range from 400 to 495 nm, with its profile rather similar to that of the core-shell particle, except that it shows a slight red shift due to the larger particle size; see the black line in Figure 4c. The NOSF comes from the recoil force due to the multipolar Fano interference, as can be understood by Figure 4d. The extinction spectra for the hollow Ag shell reveal that the Fano dip is also attributed to the broad-dipole-mode-intermediated

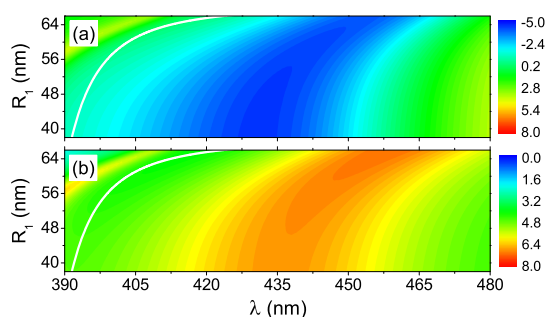


**Figure 5.** Phase diagrams of longitudinal optical force  $F_z$  acting on a Au–Ag core–shell nanoparticle (a) and the corresponding extinction efficiency  $Q_{\text{ext}}$  (b) with respect to the incident wavelength  $\lambda$  and the core radius  $R_1$ , exhibiting the red shift of the NOSF phase with an increase in particle radius, in accord with the Fano interference. The optical force is in units of pN. The outer (shell) radius is fixed at  $R_2 = 80$  nm. All other parameters are the same as in Figure 1. The white line denotes the positions of the Fano dip due to the quadrupole–octupole interference mediated by the dipole mode, which may serve roughly as a guide to the eyes for the onset of the NOSF phase for the core–shell plasmonic nanoparticle when it is illuminated by a zeroth-order TM-polarized Bessel beam specified in the caption of Figure 1.

narrow quadrupole and octupole coupling, as illustrated in Figure 4d.

It should be pointed out that in this paper we work with spherical particles, because the numerical calculation can be performed to very high precision based on the generalized Mie theory. For more general nanostructures, the analysis can be performed within the framework of multipole expansion, where the incident term  ${}^I F_z$  can be written as a sum of tensor products of multipoles with multiple gradients of incident fields, while the recoil term  ${}^R F_z$  is a sum of tensor products of adjacent multipoles.<sup>61</sup> Physically, a Fano resonance corresponds to a simultaneous excitation of multiple multipoles. It therefore augments  ${}^R F_z$  remarkably in magnitude, rendering a big opportunity to generate an NOSF.

The Fano resonance-induced NOSF is characterized by its adjustability, arising from the flexible tailorability of the Fano resonance by particle morphology such as size, structure, and shape. Therefore, it allows for tailoring the scattering force and adds significantly to the toolbox of optical manipulation such as size-selective trapping and sorting on plasmonic particles and/or nanostructures. Figure 5 gives such an example by presenting phase diagrams of longitudinal optical force  $F_z$  and extinction efficiency  $Q_{\text{ext}}$  with respect to the incident wavelength and core radius  $R_1$  for a Au–Ag core–shell nanoparticle with a fixed outer radius  $R_2 = 80$  nm, which are, nonetheless, tailorable by tuning the radius  $R_1$  of the Au core. The parameter space corresponding to the NOSF phase and the phase of positive optical scattering force (POSF) can be discriminated in Figure 5a, and, interestingly, a transition from POSF phase to NOSF phase is discerned,

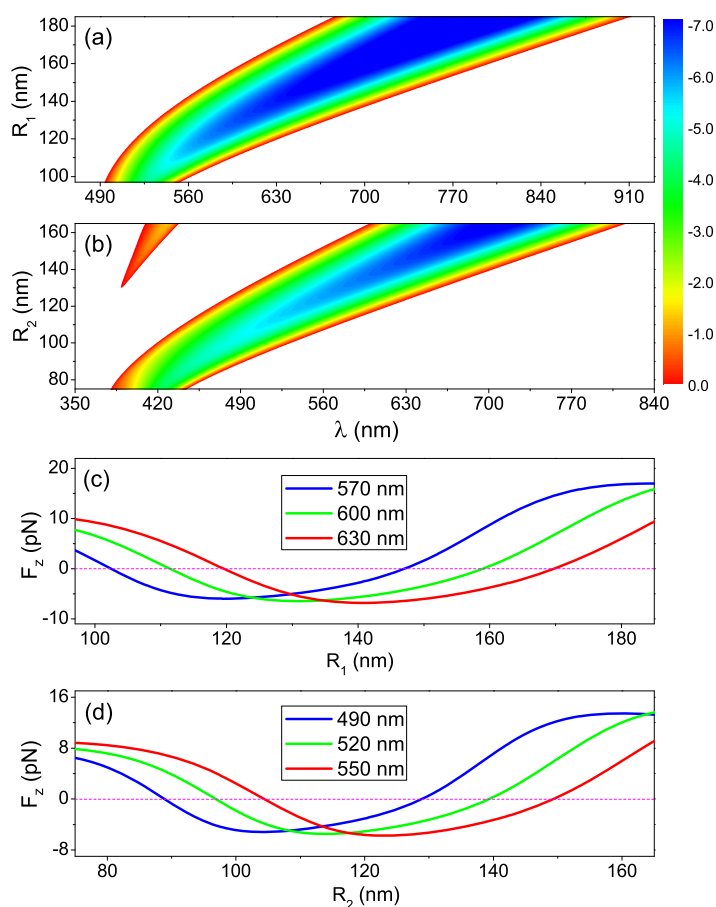


**Figure 6.** Phase diagrams of the longitudinal optical force in units of pN with respect to the incident wavelength and the particle size for a homogeneous Au nanoparticle with radius  $R_1$  (a) and for a hollow Ag nanoparticle with an empty core radius fixed at  $R_1 = 40$  nm and an outer radius  $R_2$  (b). White regions indicate the parameter space for the POSF phase, while colored regions denote the parameter space to implement the NOSF phase. The tunability of the optical scattering force by particle size is manifested by the red shift of the NOSF phase with the increase of the particle size. The red region in the upper-left corner of panel b denotes a NOSF phase resulting from the interference of higher order multipoles up to electric hexadecapole. The longitudinal optical forces at typical wavelengths of  $\lambda = 570$ , 600, and 630 nm in panel a and  $\lambda = 490$ , 520, and 550 nm in panel b are plotted versus particle size in panels c and d, respectively, to illustrate the particle selection effect of the pulling and pushing forces. All other parameters are the same as in Figure 1.

signifying a reversal of optical action from repulsion to attraction. A Fano dip corresponding to a variant Au–Ag core–shell nanoparticle is marked by the white line, lying close to the high-frequency side of the NOSF phase, implying a crucial role of Fano interference for realizing the NOSF phase, in good agreement with Figures 2 and 3. One can also observe that the NOSF phase shrinks and exhibits a red shift as the core radius increases, in accord with the tendency of the Fano dip. This core-size-induced shift originates physically from the plasmon resonances of both Au core and Ag shell. When the core size is large enough, the plasmon resonance of the Au dominates the hybridized coupling resonance over the Ag shell. So an increase of core size leads to a red shift of the NOSF phase along with the multipolar Fano resonance, despite the fact that under the same circumstances the Ag shell has a more intense

resonance than that of Au.<sup>79</sup> On the contrary, as the core size decreases, a blue shift takes place because the plasmon mode of Ag plays an increasingly predominant role in the same situation. The interaction between the two plasmon modes can be visually understood with the plasmon hybridization method.<sup>80</sup> This typical paradigm indicates that engineering composite plasmonic nanoparticles enables a tailorable Fano resonance and NOSF phase, thus facilitating optical manipulation.

The flexible tunability of the Fano interference-induced NOSF is likewise obvious for other plasmonic nanoparticles apart from the core–shell ones, as is illustrated *via* the phase diagrams of the longitudinal optical force with respect to the incident wavelength and the particle size, shown in Figures 6a and b, for homogeneous Au and hollow Ag nanoparticles. The white and colored regions in Figure 6 indicate

the POSF and NOSF phase, respectively. Figure 6a demonstrates a conspicuous red shift of the NOSF phase and an enhancement of the NOSF with an increase in particle size. This comes from the fact that the plasmon resonance of the Au particle is easily tuned by particle size, as is the Fano resonance. The similar phenomenon can also be observed for a hollow Ag nanoparticle, as shown in Figure 6b, where the empty core radius is fixed at  $R_1 = 40$  nm. As the outer radius  $R_2$  increases, the NOSF phase also shows a red shift due to that of the Fano interference. This tunable characteristic of the Fano resonance-induced NOSF can be anticipated for other plasmonic nanostructures.

Interestingly, for the larger hollow Ag nanoparticles, there appear multiple entrances from the POSF phase to the NOSF phase, as indicated by the colored region in the upper-left corner of Figure 6b. The upper NOSF phase originates from the even higher order Fano interference up to electric hexadecapole. A similar phenomenon has also been observed for the transverse optical binding force, where the multiple sign reversals occur due to the Fano interference between the dipole and higher multipole modes.<sup>53</sup> In addition, the concept of phase diagrams shown in Figures 6a and b can be used to implement the particle selection as illustrated in Figures 6c and d for Au and hollow Ag nanoparticles, respectively. As the NOSF pulls backward while the POSF pushes forward, particles with different sizes are expected to be sorted, and those within a specified size range can be selected. The mechanism is quite different from the particle sorting that requires two counterpropagating beams with different incident wavelengths,<sup>81</sup> offering an additional degree of freedom to optical manipulation of plasmonic particles.

Finally, from the experimental point of view, the heating effect might be an inevitable issue due to the absorption of metallic nanoparticles.<sup>82,83</sup> The material absorption induces a temperature increase of the illuminated particles, which, in high light intensity, can even yield bubbling of the surrounding liquid and thus can ruin stable optical manipulation. To analyze this effect in our situation, we have estimated the temperature rise ( $\Delta T$ ) on the particle surface by<sup>82,83</sup>

$$\Delta T = \frac{P_{\text{abs}}}{4\pi RK_w} \quad (3)$$

where  $P_{\text{abs}}$  is the absorption power,  $R$  is the radius of the nanoparticle, and  $K_w$  is the thermal conductivity of water. For a reliable estimation, we have compared all the parameters in the present work with the experimental data<sup>82</sup> and retrieved the temperature increase,  $\Delta T$ . For the 80 nm Au–Ag core–shell nanoparticle, 110 nm Au nanoparticle, and 90 nm hollow Ag nanoparticle considered in Figures 2 and 3, the

temperature rise ( $\Delta T$ ) is estimated to be about 100, 300, and 65 °C, respectively, at the frequency where maximum NOSF occurs. The Au nanoparticle exhibits the largest temperature rise due to its large particle size and strong material loss. Nonetheless, even if  $\Delta T$  reaches 300 °C, explosive boiling is not observed in the experiment.<sup>83</sup> In addition, the stable optical trap is reported for a larger Au nanoparticle with a radius of 127 nm<sup>78,84</sup> and Ag nanoparticle with a radius of 138 nm.<sup>85</sup> So we may expect the NOSF-based manipulation to remain feasible. More importantly, in the present proof-of-concept demonstration, we have assumed a relatively high intensity to show a conspicuous effect. For practical application, an optical force close to 1 pN could still come into play, which allows for a decrease of manipulating light intensity by a factor of 8 and thus diminishes the temperature rise ( $\Delta T$ ) to about 37 °C even for a 110 nm Au particle that has the largest absorption, while for the other two cases,  $\Delta T$  is around 10 °C. In this case, the disturbance of the heating effect on the practical implementation of the NOSF is expected to be largely eliminated in the aqueous environment.

## CONCLUSIONS

In conclusion, we have theoretically demonstrated that the Fano resonance provides a powerful way to tailor the optical scattering force on plasmonic particles and, in particular, can even induce a net NOSF on plasmonic nanoparticles when an appropriate incident optical beam is adopted. In our study, a zeroth-order Bessel beam of TM polarization serves as an example for an optical beam to achieve an NOSF, while the plasmonic particles can be core–shell, homogeneous, or hollow nanoparticles. The underlying physical mechanism of the Fano interference-induced NOSF lies in the fact that multiple multipoles are simultaneously excited, which is a signature of the Fano resonance, substantially enhances the forward scattering *via* the Fano interference, leading to a dramatically increased backward recoil force that beats the forward incident force. As a result, other nanostructures exhibiting Fano interference can be expected to undergo a net NOSF as well, based on a similar physical mechanism. As Fano resonances have been identified in many fields ranging from atomic physics<sup>25,26</sup> to classical optics,<sup>27,28</sup> the so-induced NOSF is anticipated to be ubiquitous provided that a suitable incident optical beam is implemented, contributing potentially as an additional degree of freedom to the development of optical manipulation. Moreover, one prominent feature of the Fano resonance-induced NOSF lies in its tunability brought about by the flexibility in engineering the Fano resonance through particle morphology such as size and shape as well as particle cluster configuration. The flexible tunability of the optical scattering force will

considerably broaden the application of optical force in nanomanipulation, in particular, in optical selection,

separation, and sorting associated with plasmonic nanoparticles.

## METHODS

**Scattering Energy.** For a zeroth-order Bessel beam of TM polarization with the magnetic field perpendicular to the propagation direction  $z$ , the electric field is given by<sup>57–59</sup>

$$\mathbf{E}_i(\rho, \phi, z) = E_0 \left[ -\frac{ik_z}{k} J_1(k_\rho \rho) \mathbf{e}_\rho + \frac{k_\rho}{k} J_0(k_\rho \rho) \mathbf{e}_z \right] e^{ik_z z} \quad (4)$$

where  $E_0$  is the amplitude of the electric field, whereas  $\mathbf{e}_\rho$ ,  $\mathbf{e}_\phi$ , and  $\mathbf{e}_z$  are three unitary base vectors associated respectively with the coordinates  $\rho$ ,  $\phi$ ,  $z$  of a cylindrical coordinate system  $(\rho, \phi, z)$ .  $k_\rho = k \sin \alpha$  and  $k_z = k \cos \alpha$  are respectively the transverse and longitudinal wave numbers, with  $\alpha$  being the cone angle<sup>58</sup> and  $k$  the wavenumber in the background medium.  $J_0(x)$  and  $J_1(x)$  represent the zeroth- and first-order Bessel functions. Here the time dependence  $e^{-i\omega t}$  has been assumed and suppressed.

In the generalized Lorenz–Mie theory,<sup>69</sup> the incident electric field  $\mathbf{E}_i$  is expanded in terms of the regular vector spherical wave functions<sup>69,77</sup>  $\mathbf{N}_{mn}^{(1)}(k, \mathbf{r})$  and  $\mathbf{M}_{mn}^{(1)}(k, \mathbf{r})$  with the origin of the spherical coordinate system  $(r, \theta, \phi)$  located at particle center, namely,

$$\mathbf{E}_i = - \sum_{n=1}^{\infty} \sum_{m=-n}^n i^{n+1} \gamma_{mn} E_0 [p_{mn} \mathbf{N}_{mn}^{(1)}(k, \mathbf{r}) + q_{mn} \mathbf{M}_{mn}^{(1)}(k, \mathbf{r})] \quad (5)$$

where

$$\gamma_{mn} = \left[ \frac{2n+1}{n(n+1)} \frac{(n-m)!}{(n+m)!} \right]^{1/2} \quad (6)$$

The partial wave expansion coefficients  $p_{mn}$  and  $q_{mn}$  for incident beam field, also known as the beam shape coefficients,<sup>69</sup> have been worked out analytically for general vector Bessel beams.<sup>70,71</sup> When the particle is placed at the beam axis of a zeroth-order TM-polarized Bessel beam, they reduce to<sup>86</sup>

$$p_{mn} = -p_n \delta_{m0}, \quad q_{mn} = 0 \quad (7)$$

where

$$p_n = \left[ \frac{2n+1}{n(n+1)} \right]^{1/2} \sin \alpha P'_n(\cos \alpha) \quad (8)$$

with  $P_n(x)$  and  $P'_n(x)$  being the Legendre polynomial and its derivative, respectively.

The scattered electric field  $\mathbf{E}_s$  from a scatterer is written in terms of the vector spherical wave functions<sup>69,77</sup>  $\mathbf{N}_{mn}^{(3)}$  and  $\mathbf{M}_{mn}^{(3)}$ :

$$\mathbf{E}_s = \sum_{n=1}^{\infty} \sum_{m=-n}^n i^{n+1} \gamma_{mn} E_0 [a_{mn} \mathbf{N}_{mn}^{(3)}(k, \mathbf{r}) + b_{mn} \mathbf{M}_{mn}^{(3)}(k, \mathbf{r})] \quad (9)$$

The partial wave expansion coefficients for the scattered field,  $a_{mn}$  and  $b_{mn}$ , can be obtained from the Mie scattering coefficients  $a_n$  and  $b_n$  of a spherical particle according to<sup>68</sup>

$$a_{mn} = a_n p_{mn}, \quad b_{mn} = b_n q_{mn} \quad (10)$$

The normalized scattering energy flow is determined by<sup>68</sup>

$$S(\theta, \phi) = \lim_{kr \rightarrow \infty} (kr)^2 \frac{|\mathbf{E}_s(r, \theta, \phi)|^2}{|E_0|^2} \quad (11)$$

When a spherical particle is positioned at the beam axis of a TM-polarized zeroth-order Bessel beam,  $S(\theta, \phi)$  is independent of  $\phi$ , due to the azimuthal symmetry.

**Optical Force.** The time-averaged optical force acting on a particle under the illumination of an arbitrary incident optical field is calculated by the integration of the Maxwell stress tensor over the outer surface  $S$  of the particle:<sup>75,76,87</sup>

$$\langle \mathbf{F} \rangle = \oint_S \hat{\mathbf{r}} \cdot \langle \mathbf{T} \rangle dS \quad (12)$$

where  $\langle \mathbf{T} \rangle$  is the time-averaged Maxwell stress tensor,<sup>75,76</sup> and  $\hat{\mathbf{r}}$  is the outward unit normal on the surface  $S$ . For a particle in the lossless background medium, the integration can be performed at a spherical surface with its radius  $R_s \rightarrow \infty$ , owing to the conservation of momentum. This allows for an explicit analytical expression in terms of partial wave expansion coefficients.<sup>86,88–90</sup> When a spherical particle is located at the beam axis of a zeroth-order TM-polarized Bessel beam, with the use of eqs 7 and 10, the longitudinal component of the optical force in Cartesian coordinates turns out to have a simple and transparent form:

$$F_z = {}^I F_z + {}^R F_z \quad (13)$$

where

$$\begin{aligned} {}^I F_z &= \frac{2\pi\epsilon_0 |E_0|^2}{k^2} \operatorname{Re} \sum_{n=1}^{\infty} [c_n (a_n p_n) p_{n+1}^* + c_{n-1} (a_n p_n) p_{n-1}^*], \\ {}^R F_z &= -\frac{4\pi\epsilon_0 |E_0|^2}{k^2} \operatorname{Re} \sum_{n=1}^{\infty} c_n [(a_n p_n) (a_{n+1}^* p_{n+1}^*)] \end{aligned} \quad (14)$$

with  $a_n$  denoting the Mie scattering coefficients<sup>68</sup> and the superscript \* representing the complex conjugate. The coefficient  $c_n$  reads

$$c_n = \left[ \frac{n(n+2)}{(2n+1)(2n+3)} \right]^{1/2} \quad (15)$$

In eq 14,  ${}^I F_z$ , termed the incident force in this paper, is a product of an electric multipole  $a_n p_n$  excited on the particle and multipole expansion coefficients  $p_{n\pm 1}$  for the incident field. It thus represents the interaction between a multipole and the incident field. Physically, it comes from the momentum of incident photons acquired by the particle when it is subject to illumination by an optical field and is therefore positive definite (pointing in the direction of light propagation). On the other hand,  ${}^R F_z$ , designated as the recoil force, is a product of adjacent multipoles,  $a_n p_n$  and  $a_{n+1} p_{n+1}$ , implying a recoil force stemming from the interference of incident field excited multipole radiation. It is this recoil term,  ${}^R F_z$ , that plays the role of attenuating the forward scattering force and even gives rise to a negative optical force,<sup>61</sup> while this term is dramatically enhanced at the Fano resonance due to the simultaneous excitation of multiple multipoles.

Finally, it is noted that both  ${}^I F_z$  and  ${}^R F_z$  are scattering forces when the particle is positioned on the beam axis of a propagation-invariant beam. In general,  ${}^I F_z$  contributes to both gradient and scattering forces, so it is termed the incident force rather than the gradient force.

**Conflict of Interest:** The authors declare no competing financial interest.

**Acknowledgment.** This work is supported by the China 973 Projects (Grant Nos. 2011CB922004 and 2013CB632701), MOE of China (B06011), National Natural Science Foundation of China (Grant Nos. 11174059 and 11274277), and the open project of SKLSP (KF2013\_6) in Fudan University. S.L. is also supported by a program for innovative research team at Zhejiang Normal University.

## REFERENCES AND NOTES

- Ashkin, A. Acceleration and Trapping of Particles by Radiation Pressure. *Phys. Rev. Lett.* **1970**, *24*, 156–159.
- Grier, D. G. A Revolution in Optical Manipulation. *Nature* **2003**, *424*, 810–816.
- Ashkin, A. *Optical Trapping and Manipulation of Neutral Particles Using Lasers*; World Scientific: Hackensack, NJ, 2006.

4. Dholakia, K.; Čizmar, T. Shaping the Future of Manipulation. *Nat. Photonics* **2011**, *5*, 335–342.
5. Padgett, M.; Bowman, R. Tweezers with a Twist. *Nat. Photonics* **2011**, *5*, 343–348.
6. Juan, M. L.; Righini, M.; Quidant, R. Plasmon Nano-Optical Tweezers. *Nat. Photonics* **2011**, *5*, 349–356.
7. Tkachenko, G.; Brasselet, E. Optofluidic Sorting of Material Chirality by Chiral Light. *Nat. Commun.* **2014**, *5*, 3577.
8. Cohen-Tannoudji, C. N. Manipulating Atoms with Photons. *Rev. Mod. Phys.* **1998**, *70*, 707–719.
9. Phillips, W. D. Laser Cooling and Trapping of Neutral Atoms. *Rev. Mod. Phys.* **1998**, *70*, 721–741.
10. Tkachenko, G.; Brasselet, E. Helicity-Dependent Three-Dimensional Optical Trapping of Chiral Microparticles. *Nat. Commun.* **2014**, *5*, 4491.
11. Svoboda, K.; Block, S. M. Optical Trapping of Metallic Rayleigh Particles. *Opt. Lett.* **1994**, *19*, 930–932.
12. Dienerowitz, M.; Mazilu, M.; Reece, P. J.; Krauss, T. F.; Dholakia, K. Optical Vortex Trap for Resonant Confinement of Metal Nanoparticles. *Opt. Express* **2008**, *16*, 4991–4999.
13. Reece, P. J.; Toe, W. J.; Wang, F.; Paiman, S.; Gao, Q.; Tan, H. H.; Jagadish, C. Characterization of Semiconductor Nanowires Using Optical Tweezers. *Nano Lett.* **2011**, *11*, 2375–2381.
14. Horneño, S.; Bastús, N. G.; Pietsch, A.; Weller, H.; Arias-Gonzalez, J. R.; Juárez, B. H. Plasmon-Exciton Interactions on Single Thermoresponsive Platforms Demonstrated by Optical Tweezers. *Nano Lett.* **2011**, *11*, 4742–4747.
15. Larsen, A. E.; Grier, D. G. Like-Charge Attractions in Metastable Colloidal Crystallites. *Nature* **1997**, *385*, 230–233.
16. Crocker, J. C.; Matteo, J. A.; Dinsmore, A. D.; Yodh, A. G. Entropic Attraction and Repulsion in Binary Colloids Probed with a Line Optical Tweezer. *Phys. Rev. Lett.* **1999**, *82*, 4352–4355.
17. Yang, A. H. J.; Moore, S. D.; Schmidt, B. S.; Klug, M.; Lipson, M.; Erickson, D. Optical Manipulation of Nanoparticles and Biomolecules in Sub-Wavelength Slot Waveguides. *Nature* **2009**, *457*, 71–75.
18. Ashkin, A.; Dziedzic, J. M.; Yamane, T. Optical Trapping and Manipulation of Single Cells Using Infrared Laser Beams. *Nature* **1987**, *330*, 769–771.
19. Zhang, H.; Liu, K. K. Optical Tweezers for Single Cells. *J. R. Soc. Interface* **2008**, *5*, 671–690.
20. Hegge, S.; Uhrig, K.; Streichfuss, M.; Kynast-Wolf, G.; Matuschewski, K.; Spatz, J. P.; Frischknecht, F. Direct Manipulation of Malaria Parasites with Optical Tweezers Reveals Distinct Functions of Plasmodium Surface Proteins. *ACS Nano* **2012**, *6*, 4648–4662.
21. Grigorenko, A. N.; Roberts, N. W.; Dickinson, M. R.; Zhang, Y. Nanometric Optical Tweezers Based on Nanostructured Substrates. *Nat. Photonics* **2008**, *2*, 365–370.
22. Jordan, P.; Cooper, J.; McNay, G.; Docherty, F. T.; Smith, W. E.; Sinclair, G.; Padgett, M. J. Three-Dimensional Optical Trapping of Partially Silvered Silica Microparticles. *Opt. Lett.* **2004**, *29*, 2488–2490.
23. Nieminen, T. A.; Asavei, T.; Hu, Y.; Persson, M.; Vogel, R.; Loke, V. L. Y.; Parkin, S. J.; Heckenberg, N. R.; Rubinsztein-Dunlop, H. Tailoring Particles for Optical Trapping and Micromanipulation: An Overview. *PIERS Online* **2008**, *4*, 381–385.
24. Jannasch, A.; Demirörs, A. F.; van Oostrum, P. D. J.; van Blaaderen, A.; Schaffer, E. Nanonewton Optical Force Trap Employing Anti-Reflection Coated, High-Refractive-Index Titania Microspheres. *Nat. Photonics* **2012**, *6*, 469–473.
25. Fano, U. Effects of Configuration Interaction on Intensities and Phase Shifts. *Phys. Rev.* **1961**, *124*, 1866–1878.
26. Miroshnichenko, A. E.; Flach, S.; Kivshar, Y. S. Fano Resonances in Nanoscale Structures. *Rev. Mod. Phys.* **2010**, *82*, 2257–2298.
27. Luk'yanchuk, B.; Zheludev, N. I.; Maier, S. A.; Halas, N. J.; Nordlander, P.; Giessen, H.; Chong, C. T. The Fano Resonance in Plasmonic Nanostructures and Metamaterials. *Nat. Mater.* **2010**, *9*, 707–715.
28. Luk'yanchuk, B. S.; Miroshnichenko, A. E.; Kivshar, Y. S. Fano Resonances and Topological Optics: An Interplay of Far- and Near-Field Interference Phenomena. *J. Opt.* **2013**, *15*, 073001.
29. Tribelsky, M. I.; Flach, S.; Miroshnichenko, A. E.; Gorbach, A. V.; Kivshar, Y. S. Light Scattering by a Finite Obstacle and Fano Resonances. *Phys. Rev. Lett.* **2008**, *100*, 043903.
30. Tribelsky, M. I.; Miroshnichenko, A. E.; Kivshar, Y. S. Unconventional Fano Resonances in Light Scattering by Small Particles. *Europhys. Lett.* **2012**, *97*, 44005.
31. Mukherjee, S.; Sobhani, H.; Lassiter, J. B.; Bardhan, R.; Nordlander, P.; Halas, N. J. Fano Shells: Nanoparticles with Built-in Fano Resonances. *Nano Lett.* **2010**, *10*, 2694–2701.
32. Peña-Rodriguez, O.; Pal, U. Au@Ag Core-Shell Nanoparticles: Efficient All-Plasmonic Fano-Resonance Generators. *Nanoscale* **2011**, *3*, 3609–3612.
33. Chen, H. J.; Shao, L.; Man, Y. C.; Zhao, C. M.; Wang, J. F.; Yang, B. C. Fano Resonance in (Gold Core)-(Dielectric Shell) Nanostructures without Symmetry Breaking. *Small* **2012**, *8*, 1503–1509.
34. Hao, F.; Nordlander, P.; Burnett, M. T.; Maier, S. A. Enhanced Tunability and Linewidth Sharpening of Plasmon Resonances in Hybridized Metallic Ring/Disk Nanocavities. *Phys. Rev. B* **2007**, *76*, 245417.
35. Hao, F.; Nordlander, P.; Sonnefraud, Y.; Dorpe, P. V.; Maier, S. A. Tunability of Subradiant Dipolar and Fano-Type Plasmon Resonances in Metallic Ring/Disk Cavities: Implications for Nanoscale Optical Sensing. *ACS Nano* **2009**, *3*, 643–652.
36. Dregely, D.; Hentschel, M.; Giessen, H. Excitation and Tuning of Higher-Order Fano Resonances in Plasmonic Oligomer Clusters. *ACS Nano* **2011**, *5*, 8202–8211.
37. Fan, J. A.; Wu, C.; Bao, K.; Bao, J.; Bardhan, R.; Halas, N. J.; Manoharan, V. N.; Nordlander, P.; Shvets, G.; Capasso, F. Self-Assembled Plasmonic Nanoparticle Clusters. *Science* **2010**, *328*, 1135–1138.
38. Yang, Z. J.; Wang, Q. Q.; Lin, H. Q. Tunable Two Types of Fano Resonances in Metal-Dielectric Core-Shell Nanoparticle Clusters. *Appl. Phys. Lett.* **2013**, *103*, 111115.
39. Zhang, S. P.; Bao, K.; Halas, N. J.; Xu, H. X.; Nordlander, P. Substrate-Induced Fano Resonances of a Plasmonic Nanocube: A Route to Increased-Sensitivity Localized Surface Plasmon Resonance Sensors Revealed. *Nano Lett.* **2011**, *11*, 1657–1663.
40. Svedendahl, M.; Käll, M. Fano Interference between Localized Plasmons and Interface Reflections. *ACS Nano* **2012**, *6*, 7533–7539.
41. Lovera, A.; Gallinet, B.; Nordlander, P.; Martin, O. J. F. Mechanisms of Fano Resonances in Coupled Plasmonic Systems. *ACS Nano* **2013**, *7*, 4527–4536.
42. Verellen, N.; Van Dorpe, P.; Huang, C. J.; Lodewijks, K.; Vandenbosch, G. A. E.; Lagae, L.; Moshchalkov, V. V. Plasmon Line Shaping Using Nanocrosses for High Sensitivity Localized Surface Plasmon Resonance Sensing. *Nano Lett.* **2011**, *11*, 391–397.
43. Le, F.; Brandl, D. W.; Urzhumov, Y. A.; Wang, H.; Kundu, J.; Halas, N. J.; Aizpurua, J.; Nordlander, P. Metallic Nanoparticle Arrays: A Common Substrate for Both Surface-Enhanced Raman Scattering and Surface-Enhanced Infrared Absorption. *ACS Nano* **2008**, *2*, 707–718.
44. Giannini, V.; Rodriguez-Oliveros, R.; Sánchez-Gil, J. Surface Plasmon Resonances of Metallic Nanostars/Nanoflowers for Surface-Enhanced Raman Scattering. *Plasmonics* **2010**, *5*, 99–104.
45. Chang, W. S.; Lassiter, J. B.; Swanglap, P.; Sobhani, H.; Khatua, S.; Nordlander, P.; Halas, N. J.; Link, S. A Plasmonic Fano Switch. *Nano Lett.* **2012**, *12*, 4977–4982.
46. Argyropoulos, C.; Chen, P. Y.; Monticone, F.; D'Aguzzo, G.; Alù, A. Nonlinear Plasmonic Cloaks to Realize Giant All-Optical Scattering Switching. *Phys. Rev. Lett.* **2012**, *108*, 263905.
47. Zhang, S.; Genov, D. A.; Wang, Y.; Liu, M.; Zhang, X. Plasmon-Induced Transparency in Metamaterials. *Phys. Rev. Lett.* **2008**, *101*, 047401.
48. Offermans, P.; Schaafsma, M. C.; Rodriguez, S. R. K.; Zhang, Y. C.; Crego-Calama, M.; Brongersma, S. H.; Rivas, J. G. Universal Scaling of the Figure of Merit of Plasmonic Sensors. *ACS Nano* **2011**, *5*, 5151–5157.

49. Pasquale, A. J.; Reinhard, B. M.; Dal Negro, L. Engineering Photonic-Plasmonic Coupling in Metal Nanoparticle Necklaces. *ACS Nano* **2011**, *5*, 6578–6585.
50. Li, Z. P.; Shegai, T.; Haran, G.; Xu, H. X. Multiple-Particle Nanoantennas for Enormous Enhancement and Polarization Control of Light Emission. *ACS Nano* **2009**, *3*, 637–642.
51. Shegai, T.; Chen, S.; Miljković, V. D.; Zengin, G.; Johansson, P.; Käll, M. A Bimetallic Nanoantenna for Directional Colour Routing. *Nat. Commun.* **2011**, *2*, 481.
52. Zhang, Q.; Xiao, J. J.; Zhang, X. M.; Yao, Y.; Liu, H. Reversal of Optical Binding Force by Fano Resonance in Plasmonic Nanorod Heterodimer. *Opt. Express* **2013**, *21*, 6601–6608.
53. Zhang, Q.; Xiao, J. J. Multiple Reversals of Optical Binding Force in Plasmonic Disk-Ring Nanostructures with Dipole-Multipole Fano Resonances. *Opt. Lett.* **2013**, *38*, 4240–4243.
54. Li, Z. P.; Zhang, S. P.; Tong, L. M.; Wang, P. J.; Dong, B.; Xu, H. X. Ultrasensitive Size-Selection of Plasmonic Nanoparticles by Fano Interference Optical Force. *ACS Nano* **2014**, *8*, 701–708.
55. Ridolfo, A.; Saija, R.; Savasta, S.; Jones, P. H.; Iatì, M. A.; Maragò, O. M. Fano-Doppler Laser Cooling of Hybrid Nanostructures. *ACS Nano* **2011**, *5*, 7354–7361.
56. Durnin, J.; Miceli, J. J., Jr.; Eberly, J. H. Diffraction-Free Beams. *Phys. Rev. Lett.* **1987**, *58*, 1499–1501.
57. Bouchal, Z.; Olivk, M. Non-Diffractive Vector Bessel Beams. *J. Mod. Opt.* **1995**, *42*, 1555–1566.
58. Turunen, J.; Friberg, A. T. Propagation-Invariant Optical Fields. *Prog. Opt.* **2010**, *54*, 1–88.
59. Mazilu, M.; Stevenson, D. J.; Gunn-Moore, F.; Dholakia, K. Light Beats the Spread: “Non-Diffracting” Beams. *Laser Photonics Rev.* **2010**, *4*, 529–547.
60. Sukhov, S.; Dogariu, A. On the Concept of “Tractor Beams”. *Opt. Lett.* **2010**, *35*, 3847–3849.
61. Chen, J.; Ng, J.; Lin, Z. F.; Chan, C. T. Optical Pulling Force. *Nat. Photonics* **2011**, *5*, 531–534.
62. Sáenz, J. J. Optical Forces: Laser Tractor Beams. *Nat. Photonics* **2011**, *5*, 514–515.
63. Sukhov, S.; Dogariu, A. Negative Nonconservative Forces: Optical “Tractor Beams” for Arbitrary Objects. *Phys. Rev. Lett.* **2011**, *107*, 203602.
64. Novitsky, A.; Qiu, C. W.; Lavrinenko, A. Material-Independent and Size-Independent Tractor Beams for Dipole Objects. *Phys. Rev. Lett.* **2012**, *109*, 023902.
65. Ruffner, D. B.; Grier, D. G. Optical Conveyors: A Class of Active Tractor Beams. *Phys. Rev. Lett.* **2012**, *109*, 163903.
66. Dogariu, A.; Sukhov, S.; Sáenz, J. J. Optically Induced “Negative Forces”. *Nat. Photonics* **2013**, *7*, 24–27.
67. Brzobohatý, O.; Karásek, V.; Šiler, M.; Chvátal, L.; Čizmar, T.; Zemánek, P. Experimental Demonstration of Optical Transport, Sorting and Self-Arrangement Using a ‘Tractor Beam’. *Nat. Photonics* **2013**, *7*, 123–127.
68. Bohren, C. F.; Huffman, D. R. *Absorption and Scattering of Light by Small Particles*; John Wiley and Sons: New York, 1983; p xiv.
69. Gouesbet, G. T-Matrix Formulation and Generalized Lorenz-Mie Theories in Spherical Coordinates. *Opt. Commun.* **2010**, *283*, 517–521.
70. Taylor, J. M.; Love, G. D. Multipole Expansion of Bessel and Gaussian Beams for Mie Scattering Calculations. *J. Opt. Soc. Am. A* **2009**, *26*, 278–282.
71. Chen, J.; Ng, J.; Wang, P.; Lin, Z. F. Analytical Partial Wave Expansion of Vector Bessel Beam and Its Application to Optical Binding. *Opt. Lett.* **2010**, *35*, 1674–1676.
72. Drude, P. Zur Elektronentheorie der Metalle. *Ann. Phys.* **1900**, *1*, 566–613.
73. Ordal, M. A.; Bell, R. J.; Alexander, R. W.; Long, L. L., Jr.; Query, M. R. Optical Properties of Fourteen Metals in the Infrared and Far Infrared: Al, Co, Cu, Au, Fe, Pb, Mo, Ni, Pd, Pt, Ag, Ti, V, and W. *Appl. Opt.* **1983**, *24*, 4493–4499.
74. Johnson, P. B.; Christy, R. W. Optical Constants of the Noble Metals. *Phys. Rev. B* **1972**, *6*, 4370–4379.
75. Jackson, J. D. *Classical Electrodynamics*, 3rd ed.; John Wiley and Sons: New York, 1999; p xxi.
76. Zangwill, A. *Modern Electrodynamics*; Cambridge Univ. Press: New York, 2012; p xiii.
77. Ng, J.; Lin, Z. F.; Chan, C. T.; Sheng, P. Photonic Clusters Formed by Dielectric Microspheres: Numerical Simulations. *Phys. Rev. B* **2005**, *72*, 085130.
78. Hansen, P. M.; Bhatia, V. K.; Harrit, N.; Oddershede, L. Expanding the Optical Trapping Range of Gold Nanoparticles. *Nano Lett.* **2005**, *5*, 1937–1942.
79. Peña-Rodríguez, O.; Pal, U. Enhanced Plasmonic Behavior of Bimetallic (Ag-Au) Multilayered Spheres. *Nanoscale Res. Lett.* **2011**, *6*, 279.
80. Prodan, E.; Radloff, C.; Halas, N. J.; Nordlander, P. A Hybridization Model for the Plasmon Response of Complex Nanostructures. *Science* **2003**, *302*, 419–422.
81. Ploschner, M.; Čizmar, T.; Mazilu, M.; Falco, A. D.; Dholakia, K. Bidirectional Optical Sorting of Gold Nanoparticles. *Nano Lett.* **2012**, *12*, 1923–1927.
82. Seol, Y.; Carpenter, A. E.; Perkins, T. T. Gold Nanoparticles: Enhanced Optical Trapping and Sensitivity Coupled with Significant Heating. *Opt. Lett.* **2006**, *31*, 2429–2431.
83. Kyrsting, A.; Bendix, P. M.; Stamou, D. G.; Oddershede, L. B. Heat Profiling of Three-Dimensionally Optically Trapped Gold Nanoparticles Using Vesicle Cargo Release. *Nano Lett.* **2011**, *11*, 888–892.
84. Hajizadeh, F.; Reihani, S. Optimized Optical Trapping of Gold Nanoparticles. *Opt. Express* **2010**, *18*, 551–559.
85. Bosanac, L.; Aabo, T.; Bendix, P. M.; Oddershede, L. B. Efficient Optical Trapping and Visualization of Silver Nanoparticles. *Nano Lett.* **2008**, *8*, 1486–1491.
86. Wang, N.; Chen, J.; Liu, S. Y.; Lin, Z. F. Dynamical and Phase-Diagram Study on Stable Optical Pulling Force in Bessel Beams. *Phys. Rev. A* **2013**, *87*, 063812.
87. Saija, R.; Denti, P.; Borghese, F.; Maragò, O. M.; Iatì, M. A. Optical Trapping Calculations for Metal Nanoparticles. Comparison with Experimental Data for Au and Ag Spheres. *Opt. Express* **2009**, *17*, 10231–10241.
88. Barton, J. P.; Alexander, D. R.; Schaub, S. A. Theoretical Determination of Net Radiation Force and Torque for a Spherical Particle Muminated by a Focused Laser Beam. *J. Appl. Phys.* **1989**, *66*, 4594–4602.
89. Farsund, Ø.; Felderhof, B. U. Force, Torque, and Absorbed Energy for a Body of Arbitrary Shape and Constitution in an Electromagnetic. *Phys. A (Amsterdam, Neth.)* **1996**, *227*, 108–130.
90. Chen, H. J.; Wang, N.; Lu, W. L.; Liu, S. Y.; Lin, Z. F. Tailoring Azimuthal Optical Force on Lossy Chiral Particles in Bessel Beams. *Phys. Rev. A* **2014**, *90*, 043850.